

## Uncertainty quantification of an empirical shell-model interaction using principal component analysis

Jordan M. R. Fox,<sup>\*</sup> Calvin W. Johnson<sup>†</sup>, and Rodrigo Navarro Perez<sup>‡</sup>  
*San Diego State University, San Diego, California 92182, USA*



(Received 19 February 2020; accepted 27 April 2020; published 12 May 2020)

Recent investigations have emphasized the importance of uncertainty quantification (UQ) in nuclear theory. We carry out UQ for configuration-interaction shell-model calculations in the  $1s$ - $0d$  valence space, investigating the sensitivity of observables to perturbations in the 66 parameters (matrix elements) of a high-quality empirical interaction. The large parameter space makes computing the corresponding Hessian numerically costly, so we compare a cost-effective approximation, using the Feynman-Hellmann theorem, to the full Hessian and find it works well. Diagonalizing the Hessian yields the principal components of the interaction: linear combinations of parameters ordered by sensitivity. This approximately decoupled distribution of parameters facilitates theoretical uncertainty propagation onto structure observables: electromagnetic transitions, Gamow-Teller decays, and dark matter-nucleus scattering matrix elements.

DOI: [10.1103/PhysRevC.101.054308](https://doi.org/10.1103/PhysRevC.101.054308)

### I. INTRODUCTION

Recent advancements in nuclear theory have emphasized the importance of theoretical uncertainty quantification (UQ) [1] with applications to, among other things, the nuclear force and effective field theory [2–7], the optical model [8,9], density functional theory [10,11], and the configuration-interaction shell model [12,13].

The shell model, which provides a useful conceptual framework for nuclear structure, can be approximately divided into *ab initio* and empirical/phenomenological approaches. *Ab initio* calculations, such as the no-core shell model [14,15], typically use forces built upon chiral effective field theory [16] and thus are arguably more fundamental and also have been subject to considerable UQ [2–7] but are limited to light nuclei, approximately mass number  $A < 16$ . Empirical shell-model calculations [17–19] have a long, rich, and successful history and, importantly, have been applied to a wide range of nuclei far beyond the  $0p$  shell, but the theoretical underpinnings are more heuristic: Individual interaction matrix elements in the laboratory frame (single-particle coordinates) are adjusted to reproduce experimental data.

(We will not consider here related but distinct methodologies such as coupled clusters [20], and we note but do not comment further on efforts to construct interactions that “look like” traditional empirical calculations but are derived with significant rigor from *ab initio* forces [21].)

Previous work on UQ in the shell model focused on  $0p$ -shell calculation: one considered a simple interaction

with only seven parameters, examining correlations using a singular-value-decomposition analysis [12]; while the other used 17 parameters but did not consider correlations between parameters [13].

Because of the broad applications and demonstrated utility of the empirical shell model, we carry out a sensitivity analysis on an widely used, “gold standard” empirical shell-model interaction, Brown and Richter’s universal  $sd$ -shell interaction, version B, or USDB [22]. Here, “ $sd$ -shell” means the valence space is limited to  $1s$  and  $0d$  single-particle orbits, with an inert  $^{16}\text{O}$  core.

In fitting their interaction, Brown and Richter followed a standard procedure [17]. They minimized the total error with respect to experiment, defined as the  $\chi^2$ -function in Eq. (5) below, by taking the first derivatives with respect to the parameters, which yield the linear response of calculated energies to perturbations of the parameters, and then carried out gradient descent on the independent parameters, here 63 two-body matrix elements and three single-particle energies. In the fit they found that about five or six linear combinations of parameters, found by singular value decomposition as we do below, were the most important. (Interesting, a similar result was found for random values of the matrix elements [23]). Brown and Richter actually produced two interactions [22], USDA, which was found by fitting the first 30 linear combinations from singular value decomposition, and USDB, found by fitting 56 linear combinations.

For a Bayesian sensitivity analysis, discussed more fully in Appendix A, one must characterize the likelihood function for model parameters. In Laplace’s approximation, one assumes the likelihood is well approximated by a Gaussian, which corresponds to a quadratic expansion in the  $\chi^2$ -function. Even so, the matrix of second derivatives of  $\chi^2$  (which, more rigorously, is the log-likelihood), or the *Hessian*, needed is quite demanding to obtain.

<sup>\*</sup>jfox@sdsu.edu

<sup>†</sup>cjohnson@sdsu.edu

<sup>‡</sup>rnavarroperez@sdsu.edu

We therefore consider a further simplification, approximating the Hessian by the same linear response (first derivatives of the energies), which are efficiently computed by the Feynman-Hellmann theorem [24,25]. As discussed below, this principal component analysis of the sensitivity is, in this approximation, singular value decomposition of the linear response. Importantly, we find that numerical corrections to the linear response matrix are small, making this approximation appealing for studying larger spaces wherein the full numerical calculation is too costly.

## II. THE EMPIRICAL CONFIGURATION-INTERACTION SHELL MODEL

We formally represent the nuclear Hamiltonian in second quantization, with  $r, s, t, u$  labeling single-particle states,

$$\hat{H} = \sum_{rs} T_{rs} \hat{a}_r^\dagger \hat{a}_s + \frac{1}{4} \sum_{rstu} V_{rs,tu} \hat{a}_r^\dagger \hat{a}_s^\dagger \hat{a}_t \hat{a}_u, \quad (1)$$

where typically one takes  $T_{rs}$  as diagonal *single-particle energies*, and the  $V_{rs,tu}$  are two-body matrix elements. As input to nuclear configuration-interaction codes, the two-body matrix elements are always coupled up to an angular momentum scalar so that the many-body angular momentum  $J$  is a good quantum number of eigenstates [17]. (To be specific, the two-body matrix elements are  $V_{JT}(ab, cd) = \langle ab; JT | \hat{V} | cd; JT \rangle$ , where  $\hat{V}$  is the nuclear two-body interaction and  $|ab; JT\rangle$  is a normalized two-body state with nucleons in single-particle orbits labeled by  $a, b$  coupled up to total angular momentum  $J$  and total isospin  $T$ .) In this paper, the single-particle energies and the coupled two-body matrix elements are the input parameters.

With the Hamiltonian Eq. (1) we want to find specific eigenpairs,

$$\hat{H}|\psi_\alpha\rangle = E_\alpha|\psi_\alpha\rangle, \quad (2)$$

in this case low-lying states with experimentally known energies. This is done by the configuration-interaction (CI) many-body method, which expands the wave function in a basis  $\{|a\rangle\}$ , usually orthonormal,

$$|\psi_\alpha\rangle = \sum_a c_{\alpha,a} |a\rangle. \quad (3)$$

Here  $\alpha$  labels the eigenstates and their observables, in particular the energy  $E_\alpha$ . For the basis we use the occupation representation of Slater determinants, that is, antisymmetrized products of single-particle states. We furthermore use basis states with fixed total  $J_z$ , also called an  $M$ -scheme basis. By computing the matrix elements of the Hamiltonian in this same basis,  $\mathcal{H}_{a,b} = \langle a | \hat{H} | b \rangle$ , the Schrödinger Eq. (2) is now a matrix eigenvalue problem, which we solve by the standard Lanczos algorithm [26] to extract the extremal eigenpairs of interest. See Refs. [17–19] for a multitude of important and interesting details and Refs. [27,28] for information on the code used.

We assume a frozen  $^{16}\text{O}$  core and use the  $1s\text{-}0d$  single-particle valence space, also called the  $sd$ -shell. Assuming both angular momentum  $J$  and isospin  $T$  are good quantum numbers, one has only three independent single-particle energies

and 63 independent two-body matrix element, for a total of 66 parameters. Because each of those parameters appears linearly in the Hamiltonian, we can write

$$\hat{H} = \sum_i \lambda_i \hat{O}_i, \quad (4)$$

where  $\hat{O}_i$  is some dimensionless one- or two-body operator. Thus, the parameters  $\lambda$  have dimensions of energy.

The set of parameters  $\lambda = \{\lambda_i\}$  we use are Brown and Richter’s universal  $sd$ -shell interaction version  $B$  (USDB) [22], which, along with its sister interaction USDA, are the current “gold standards” for empirical  $sd$ -shell calculations. The present study seeks to extend this model by computing theoretical uncertainties on model parameters and shell-model observables [29,30]. While the parameter vector  $\lambda$  is formally considered a random variable, note that all calculations are performed about the USDB values.

An important nuance in using the USDB parameters is that while the single-particle energies are fixed, the two-body matrix elements are scaled by  $(A_0/A)^{0.3}$ , where  $A$  is the mass number of the nucleus, and  $A_0$  is a reference value, here = 18. We account for this by modifying Eq. (4) as  $\hat{H} = \sum_i \lambda_i (A_0/A)^{0.3} \hat{O}_i$  (but only for the two-body matrix elements), so that we implicitly varied the parameters fixed at  $A = 18$ .

Experimental energies in this paper are the same used in the original fit of the USDB Hamiltonian: absolute energies, relative to the  $^{16}\text{O}$  core and with Coulomb differences subtracted, of 608 states in 77 nuclei with  $A = 21\text{--}40$ . The data excludes any experimental uncertainties greater than 200 keV, and most are smaller, on the order of 10 keV.

In the rest of this paper, we estimate the uncertainty in the USDB parameters and, from those, estimate uncertainties in observables such as energies, probabilities for selected electromagnetic and weak transitions, and for a matrix element relevant to dark matter direct detection.

## III. SENSITIVITY ANALYSIS

Our analysis can be cast in terms most physicists are familiar with, see, e.g., Refs. [1,31–33]. In the Appendix we discuss the relationship to Bayesian analysis, giving a more rigorous starting point and setting the stage for more sophisticated analyses.

We begin with the  $\chi^2$  function of parameters  $\lambda$ , which is the usual sum of squared residuals over  $N$  data:

$$\chi^2(\lambda) = \sum_{\alpha=1}^N \left( \frac{E_\alpha^{\text{SM}}(\lambda) - E_\alpha^{\text{exp}}}{\Delta E_\alpha} \right)^2. \quad (5)$$

In addition,  $E_\alpha^{\text{exp}}$  is the experimental excitation energy given in the data set and  $E_\alpha^{\text{SM}}(\lambda)$  is the shell-model calculation for that energy using the parameters  $\lambda$ . The total uncertainty  $\Delta E_\alpha$  on the residual is expressed as experimental uncertainty  $\Delta E_\alpha^{\text{exp}}$  and some *a priori* theoretical uncertainty  $\Delta E^{\text{th}}$  added in quadrature:

$$\Delta E_\alpha^2 = (\Delta E^{\text{th}})^2 + (\Delta E_\alpha^{\text{exp}})^2 \quad (6)$$

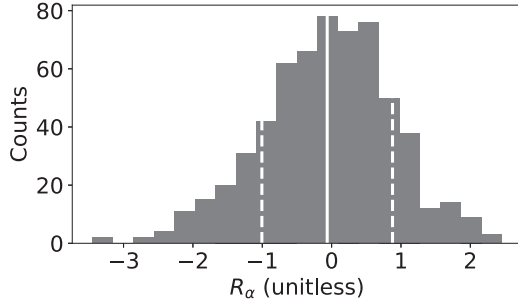


FIG. 1. Histogram of energy residuals  $R_\alpha = [E_\alpha^{\text{SM}}(\lambda_{\text{USDB}}) - E_\alpha^{\text{exp}}]/\Delta E_\alpha$ .

Here we introduce  $\Delta E^{\text{th}}$  as an estimated uncertainty on the shell-model predictions of the data. We assume it is independent of the level, that is, of  $\alpha$ , and fix it by requiring the reduced sum of squared residuals  $\chi_\nu^2 = \frac{1}{\nu}\chi^2 \approx 1$  [32], which gives us  $\Delta E^{\text{th}} \approx 150$  keV. Here  $\nu$  is the number of degrees of freedom: the number of data points minus the number of parameters. In their original paper, Brown and Richter set  $\sigma^{\text{th}}$  (equivalent to our  $\Delta E^{\text{th}}$ ) = 0.1 MeV as “close to the rms value” they eventually found, 126 keV [22].

Before proceeding with the sensitivity analysis, it is important to test the distribution of residuals  $R_\alpha = [E_\alpha^{\text{SM}}(\lambda_{\text{USDB}}) - E_\alpha^{\text{exp}}]/\Delta E_\alpha$ , shown in Fig. 1, since we will approximate it to be normally distributed (equivalent to Laplace’s approximation discussed in Appendix A). We employ two statistical tests

of normality: Kolmogorov-Smirnov [34] (KS-test) and tail-sensitive [35,36] (TS-test); the former is a typical test of overall normality, while the latter is more sensitive to features in the tails of the distribution. Each test returns a  $p$ -value: we adopt the traditional significance threshold of  $p > 0.05$  as no significant evidence for deviations from the standard normal distribution. This is sometimes colloquially referred as agreement between the empirical and theoretical distributions. To visualize these tests of normality, we show a rotated quantile-quantile (Q-Q) plot of the residuals  $R_\alpha$  in Fig. 2. The residuals appear to have a nearly normal distribution, and indeed the KS-test returns a  $p$  value of 0.15. This validates our implementation of Laplace’s approximation. However, the more sensitive TS-test returns a  $p$  value of 0.02, indicating that the tails of the residual distribution contain sufficient nonnormal features as to warrant a more detailed study in future work.

Under the assumption the errors have a normal distribution,  $\chi^2$  is well-approximated by quadratic function in  $\lambda$ , and we can compute the Hessian  $H$ , or the second derivative of  $\chi^2$ , that is,

$$H_{ij} = \frac{1}{2} \frac{\partial^2}{\partial \lambda_i \partial \lambda_j} \chi^2. \quad (7)$$

Note that we write the Hessian matrix as  $H$ , and the Hamiltonian operator as  $\hat{H}$ . We can simplify this expression to put it in terms of eigenenergies:

$$\frac{\partial^2 \chi^2}{\partial \lambda_i \partial \lambda_j} = \sum_{\alpha=1}^N \frac{2}{(\Delta E_\alpha)^2} \left[ \frac{\partial E_\alpha^{\text{SM}}}{\partial \lambda_i} \frac{\partial E_\alpha^{\text{SM}}}{\partial \lambda_j} + (E_\alpha^{\text{SM}} - E_\alpha^{\text{exp}}) \frac{\partial^2 E_\alpha^{\text{SM}}}{\partial \lambda_i \partial \lambda_j} \right], \quad (8)$$

so that

$$H_{ij} = \sum_{\alpha=1}^N \frac{1}{(\Delta E_\alpha)^2} \frac{\partial E_\alpha^{\text{SM}}}{\partial \lambda_i} \frac{\partial E_\alpha^{\text{SM}}}{\partial \lambda_j} + \sum_{\alpha=1}^N \frac{(E_\alpha^{\text{SM}} - E_\alpha^{\text{exp}})}{(\Delta E_\alpha)^2} \frac{\partial^2 E_\alpha^{\text{SM}}}{\partial \lambda_i \partial \lambda_j}. \quad (9)$$

The first term in this expression dominates, so we define the *approximate Hessian A* as follows:

$$H_{ij} \approx \sum_{\alpha=1}^N \frac{1}{(\Delta E_\alpha)^2} \frac{\partial E_\alpha^{\text{SM}}}{\partial \lambda_i} \frac{\partial E_\alpha^{\text{SM}}}{\partial \lambda_j} \equiv A_{ij}. \quad (10)$$

This approximation is good if the cross-derivative is small, for example if the energies were exactly linear in the parameters, or alternatively if the residual is small (meaning the model is good). Furthermore, the calculation of  $E_\alpha^{\text{SM}}$  is made with the optimized USDB parameters, therefore the term multiplying the cross-derivative should on average be close to zero. The second term contains the cross-derivative, and this is more challenging to calculate, especially considering the size of the parameter-space.

Note that the energy matrix element is nonlinear in  $\lambda$  due to dependence in the wave function. If one were to ignore this dependence, then we call this the *linear model*

*approximation*,

$$E = \langle \psi(\lambda) | \hat{H}(\lambda) | \psi(\lambda) \rangle \approx \langle \psi | \hat{H}(\lambda) | \psi \rangle = \sum_{i=1} \lambda_i \langle \psi | \hat{O}_i | \psi \rangle. \quad (11)$$

Under the linear model approximation, any cross-derivative term is zero and thus the “approximate” Hessian above would be equal to the full Hessian:  $A = H$ .

To compute the derivatives of the energies, in Eq. (10), we use the Feynman-Hellmann theorem,

$$\frac{\partial E_\alpha^{\text{SM}}(\lambda)}{\partial \lambda_i} = \left\langle \psi_\alpha \left| \frac{d\hat{H}}{d\lambda_i} \right| \psi_\alpha \right\rangle = \langle \psi_\alpha | \hat{O}_i | \psi_\alpha \rangle, \quad (12)$$

where the Hamiltonian Eq. (4) is linear in  $\lambda_i$ . (These first derivatives are Jacobians [1].) Thus, for the first derivatives in Eq. (10), we can simply evaluate expectation values of the individual one- and two-body operators.

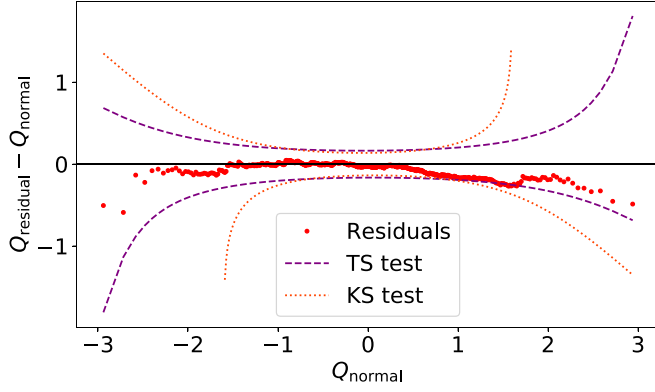


FIG. 2. Rotated quantile-quantile (Q-Q) plot of energy residuals  $(E_\alpha^{\text{SM}}(\lambda_{\text{USDB}}) - E_\alpha^{\text{exp}}) / \Delta E_\alpha$  with respect to standard normal distribution. The dashed and dotted lines in the Q-Q plot show the boundaries of TS and KS-tests, respectively. Deviation from the horizontal axis indicates nonnormal deviations in the data. The residual points crossing the dashed purple line around  $Q_{\text{normal}} \approx 1.5$  corresponds to the low  $p$  value returned by the TS-test. (A brief explanation of Q-Q plots can be found in the Appendix.)

While the full numerical calculation of the Hessian is quite costly, we can numerically compute the cross-derivative term in Eq. (9) with a simple finite difference approximation of the second derivative, so as to achieve a better approximation to the exact Hessian,

$$\frac{\partial^2 E_\alpha^{\text{SM}}}{\partial \lambda_i \partial \lambda_j} = \frac{1}{2\epsilon} \left[ \frac{\partial E_\alpha^{\text{SM}}(\lambda_j^+)}{\partial \lambda_i} - \frac{\partial E_\alpha^{\text{SM}}(\lambda_j^-)}{\partial \lambda_i} \right] + \mathcal{O}(\epsilon^2). \quad (13)$$

Here,  $E_\alpha^{\text{SM}}(\lambda_j^\pm)$  is the  $\alpha$ th energy evaluated using USDB parameters with the  $j$ -th value perturbed by  $\pm\epsilon$ . Inserting into Eq. (9), we denote the resulting numerically corrected approximate Hessian matrix as  $A_{\text{num}}$ ,

$$[A_{\text{num}}]_{ij} \equiv [A]_{ij} + \sum_{\alpha=1}^N \frac{(E_\alpha^{\text{SM}}(\lambda) - E_\alpha^{\text{exp}})}{(\Delta E_\alpha)^2} \frac{1}{2\epsilon} \times \left[ \frac{\partial E_\alpha^{\text{SM}}(\lambda_j^+)}{\partial \lambda_i} - \frac{\partial E_\alpha^{\text{SM}}(\lambda_j^-)}{\partial \lambda_i} \right]. \quad (14)$$

We tested their importance by evaluating with  $\epsilon \approx 0.1$ . The the resulting eigenvalues of  $A$  and  $A_{\text{num}}$ , shown in Table I, are very similar, indicating that while the numerical corrections terms are individually nonzero, the total contributions average to very small contributions.

Thus,  $A$  is in fact a very good approximation to the full Hessian matrix and, in what follows, we find that propagation of uncertainties onto observables are almost independent of the numerical correction. This also implies that the linear model approximation [Eq. (11)] is a good approximation.

#### PCA transformation

The Hessian, whether exact ( $H$ ) or approximate ( $A$ ), allows us to determine the uncertainty in parameters, discussed in more detail in Sec. IV, and in particular the uncorrelated uncertainties. Transforming the Hessian  $UHU^T = D$ , where

TABLE I. Statistics of linear-combinations of USDB matrix elements, or *principle component analysis* (PCA) parameters. The eigenvalues of the approximate Hessian matrix  $A$  we denote as  $[\Delta]_{ii}$ , which is the sensitivity of the  $i$ th PCA parameter, and  $\sigma_i$  is the corresponding uncertainty. Thus, the most sensitive PCA parameter is constrained to within 290 eV. Likewise, the eigenvalues of the numerically corrected approximate Hessian matrix  $A_{\text{num}}$  we denote as  $[\Delta_{\text{num}}]_{ii}$ , and  $[\sigma_{\text{num}}]_i$  is the corresponding uncertainty. Note that for the most sensitive PCA parameters, the numerical correction effectively leaves the standard deviations unchanged.

$i$	$[\Delta]_{ii}$ (MeV <sup>-2</sup> )	$\sigma_i$ (keV)	$[\Delta_{\text{num}}]_{ii}$ (MeV <sup>-2</sup> )	$[\sigma_{\text{num}}]_i$ (keV)
1	11 785 000	0.29	11 785 500	0.29
2	393 000	1.6	393 600	1.6
3	79 100	3.5	78 810	3.5
4	71 200	3.7	70 800	3.7
5	22 200	6.7	22 220	6.7
6	6357	13	6357	13
7	5200	14	5175	14
8	3600	17	3590	17
9	3270	17	3261	17
10	3050	18	3035	18
...	...	...	...	...
64	10.6	307	<1	>1000
65	7.71	360	<0.1	>3000
66	3.16	562	<0.1	>3000

$D$  is diagonal, or its approximation,

$$WAW^T = \Delta, \quad (15)$$

where  $\Delta \approx D$  is also diagonal, provides a transformation from the original parameters  $\lambda$  to new linear combinations of parameters,

$$\mu = W\lambda. \quad (16)$$

This is simply *principal component analysis* (PCA) of the Hessian, and so we call  $\mu$  the PCA parameters. In terms of our approximate Hessian, we can also understand this as a singular value decomposition (SVD) of the linear response  $J_{\alpha i} = \partial E_\alpha / \partial \lambda_i$ . More formally, we approximate  $H \approx A = J^T \Sigma^{-2} J$ , where  $\Sigma$  is the diagonal matrix of uncertainties on energies,  $\Sigma_{\alpha\beta} = \delta_{\alpha\beta} \Delta E_\alpha$ ; but, as is nearly true,  $\Delta E_\alpha \approx \Delta E_\alpha^{\text{th}}$  and hence  $A \approx (\Delta E^{\text{th}})^{-2} J^T J$ ; then it should be clear that the eigenvalues of  $A$  are proportional to the SVD eigenvalues of  $J$ . Thus, the eigenvalues found in  $\Delta$ , presented in Table I and plotted in Fig. 3, allow us to determine the most important linear combinations of parameters to the fit.

#### IV. EVALUATING UNCERTAINTIES

The parameter covariance matrix is simply the inverse of the Hessian matrix, which we have approximated as

$$C(\lambda) = H^{-1} \approx A^{-1} = W^T \Delta^{-1} W. \quad (17)$$

The naive variance of the original parameters  $\lambda$  is given by the diagonals of the covariance matrix, so that  $\sigma(\lambda_i) = \sqrt{C_{ii}}$ . This, however, ignores correlations between parameters and

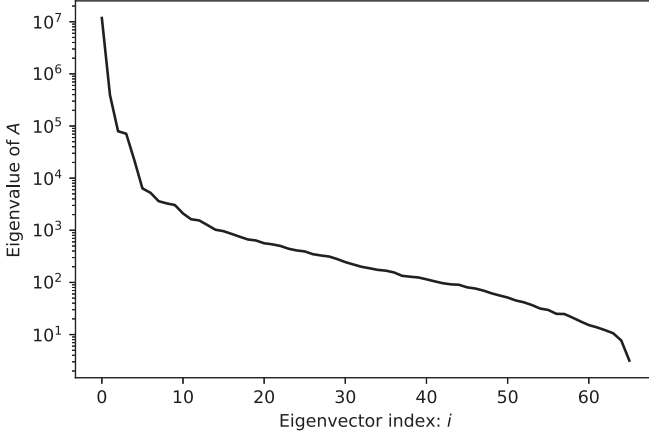


FIG. 3. Ordered eigenvalues of the approximate Hessian  $A$ , which equal the diagonal elements of  $\Delta$ . The eigenvalues are interpreted as the sensitivity of the corresponding linear combination or principal components of matrix elements (PCA-parameter). The first PCA-parameter carries 95% of the total sensitivity, and the first 5 PCA-parameters carry 99.6% of the sensitivity.

thus is an incomplete description of parameter uncertainties. A better approach is to compute variances from the diagonalized Hessian matrix, and thus obtaining uncorrelated uncertainties on the PCA parameters,  $\sigma(\mu) = 1/\sqrt{\Delta_{ii}}$ . These we give in Table I and plot in Fig. 3. Here one sees the first few PCA parameters have very large sensitivity, and indeed the first 10 carry over 99.8% of the total; it is well-known lore in the nuclear shell-model community the fit of USDB and similar empirical interactions are dominated by only a few linear combinations, which here define the PCA parameters. Table I, in fact, demonstrates these parameters must be known to within a few keV or better; on the other hand 23 PCA parameters have uncertainties of 100–500 keV. At this point, it is important to remember that these variabilities are with respect to experimental data that only includes energies, so these low-variability PCA parameters could in principle be tuned to fit the interaction to various other observables without disrupting the fit to energies.

If the uncertainties in the principal components  $\mu$  are independent, then the propagation of uncertainties is straightforward. For any observable  $X$ ,

$$\sigma^2(X) = \sum_i \left( \frac{\partial X}{\partial \mu_i} \right)^2 \sigma^2(\mu_i). \quad (18)$$

Using Eq. (16),

$$\frac{\partial X}{\partial \mu_i} = \sum_j W_{ij} \frac{\partial X}{\partial \lambda_j} \quad (19)$$

and so

$$\sigma^2(X) = \sum_i \sigma^2(\mu_i) \sum_{jk} \frac{\partial X}{\partial \lambda_j} W_{ij} \frac{\partial X}{\partial \lambda_k} W_{ik} = \mathbf{g}^T \mathbf{C} \mathbf{g}, \quad (20)$$

where  $g_i = \partial X / \partial \lambda_i$  is the linear response of any observable to perturbations in the original parameters. This is particularly useful in the case of energies, where we already have the linear

TABLE II. States in experimental energy data, shown in order of descending uncertainty  $\sigma$  (high-variability on top, low-variability on bottom).

Nucleus	$J_n^\pi$	$T$	$E^{\text{exp}} - E^{\text{SM}}$ (keV)	$\sigma$ (keV)
$^{30}\text{Si}$	$1_1^+$	1	-114	851
$^{39}\text{K}$	$1/2_1^+$	1/2	-189	785
$^{25}\text{F}$	$5/2_1^+$	7/2	-312.1	743
$^{38}\text{K}$	$1_1^+$	0	-355.9	686
$^{27}\text{Al}$	$11/2_1^+$	1/2	-52.9	615
...	...	...	...	...
$^{24}\text{Mg}$	$6_1^+$	0	156.1	156
$^{20}\text{Ne}$	$6_1^+$	0	-223.2	154
$^{23}\text{Na}$	$11/2_1^+$	1/2	-15.3	153
$^{28}\text{Mg}$	$2_1^+$	2	19.3	153
$^{17}\text{O}$	$5/2_1^+$	1/2	218.3	142

response, thanks to the Feynman-Hellmann theorem. For a discussion of some of the subtleties, see Appendix B.

For other observables, we do not use Eq. (20) directly. Instead, we generate perturbations in USDB by generating perturbations in the PCA parameters  $\delta\mu$  with a Gaussian distribution with width  $\sigma(\mu_i)$  given by Table I. Because the uncertainties are independent, or nearly so, in the PCA parameter representation, it is safe to generate the perturbations independently. We then transform back to the original representation of the matrix elements and read into a shell-model code [27,28], find eigenpairs, and evaluate the reduced transition matrix element for one-body transition operators. We sampled at least 1000 sets of parameters, which gives sufficient convergence of the resulting set of matrix elements: assuming the transition strengths  $B_i$  are normally distributed with respect to small perturbations in the Hamiltonian, we take the theoretical uncertainty  $\sigma(B_i)$  as equal to the standard deviation of the set of samples. Previous works have demonstrated convergence with similar approaches and an even smaller number of samples. In Ref. [37] the statistical uncertainty in the binding energy of  $^3\text{H}$  was quantified using 250 samples of an interaction with about 40 parameters, resulting in  $\sigma(B) = 15$  keV. The same result was later reproduced in Ref. [38] using only 33 samples.

## Results

For the energies used in the fit, we already have the elements of  $\vec{g}$  saved from computing the approximate Hessian, so this calculation is cheap. We can thus estimate covariance in the computed energies  $C_E$  by expanding this expression to a matrix equation,

$$C_E = \mathbf{J} \mathbf{C}_\lambda \mathbf{J}^T. \quad (21)$$

Results for some of these estimated uncertainties are given in Table II. Using these estimates, 75% of shell-model energies are within  $1\sigma$  of experiment, and 96% are within  $3\sigma$ ; these are close to the standard normal quantiles of 68% and 99%, respectively, so we conclude that these theoretical uncertainties are sensible. Akin to the original sensitivity analysis of

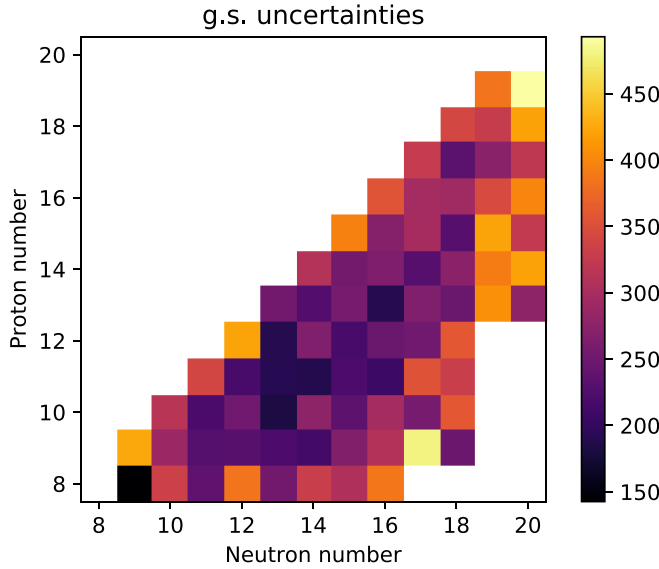


FIG. 4. Estimated  $1\sigma$  uncertainties of ground-state fit energies in units of keV.

fit energies [22], Fig. 4 shows theoretical  $1\sigma$  uncertainties on ground-state binding energies. We refer the reader to Ref. [22] for comparison to uncertainty plots, in particular, Fig. 10 of that paper. While this description of uncertainties on the fitted energies may be useful, we also note that they are in a sense tautological: the energy covariance  $C_E$  is related to the energy uncertainties in Eq. (6) by a coordinate transformation. An algebraic explanation is given in Appendix B.

We also computed the uncertainties in selected transitions. The uncertainty bands presented in all transition strength calculations correspond to the 16th–84th percentiles; for normal

distributions this is precisely the  $1\sigma$  uncertainty band, but we find many computed transition strengths have asymmetric distributions (especially those with small B values). This, along with reporting median rather than mean, gives a more accurate description of uncertainty.

Following Ref. [30], we compute reduced transition strengths  $B(E2)$  for several low-lying transitions in  $^{26}\text{Mg}$  and  $^{26}\text{Al}$ , shown in Fig. 5 and 6, respectively. The one-body electric quadrupole operator matrix elements were computed assuming harmonic oscillator radial wave functions with oscillator length  $b = 1.802$  [18] and effective charges  $e_p = 1.36$ ,  $e_n = 0.45$ , which were obtained by a least-squares fit [29]. While some values are close to experiment, others differ significantly. The  $B(E2)$  values are quadratically dependent upon both the oscillator length and the effective charges, and can be quite sensitive to small changes in the interaction matrix elements [30].

For  $^{26}\text{Mg}$ , in Fig. 5, the median values and uncertainty intervals for our selected transitions are  $2_1^+ \rightarrow 0_1^+$ :  $63.7^{+0.78}_{-0.83}$ ,  $2_2^+ \rightarrow 0_1^+$ :  $3.46^{+0.55}_{-0.52}$ ,  $0_2^+ \rightarrow 2_1^+$ :  $1.15^{+0.33}_{-0.29}$ , and  $2_4^+ \rightarrow 0_1^+$ :  $0.96^{+0.18}_{-0.18}$ , all in units of  $e^2\text{fm}^4$ , while for  $^{26}\text{Al}$ , in Fig. 6 the median values and uncertainty intervals for our selected transitions are  $3_1^+ \rightarrow 5_1^+$ :  $52.04^{+0.99}_{-1.0}$ ,  $1_2^+ \rightarrow 3_1^+$ :  $54.47^{+4.19}_{-4.92}$ ,  $2_2^+ \rightarrow 0_1^+$ :  $56.63^{+1.26}_{-1.16}$ ,  $1_3^+ \rightarrow 3_1^+$ :  $0.53^{+2.53}_{-0.49}$ ,  $3_2^+ \rightarrow 5_1^+$ :  $0.017^{+0.041}_{-0.015}$ , and  $3_3^+ \rightarrow 1_1^+$ :  $11.38^{+2.82}_{-2.53}$ .

Magnetic dipole reduced transition strengths  $B(M1)$  distributions for  $^{18}\text{F}$  and  $^{26}\text{Al}$  are shown in Figs. 7 and 8, respectively. We used bare gyromagnetic factors, with no corrections for exchange currents. Like the  $B(E2)$  values, some of the transitions are close to experiment, while the  $0_1^+ \rightarrow 1_1^+$  in  $^{18}\text{F}$  is quite far away. For  $^{18}\text{F}$ , in Fig. 7, the median values and uncertainty intervals for our selected transitions are  $0_1^+ \rightarrow 1_1^+$ :  $17.13^{+0.19}_{-0.21}$ ,  $1_2^+ \rightarrow 0_1^+$ :  $0.31^{+0.076}_{-0.068}$ , and  $3_2^+ \rightarrow 2_1^+$ :  $0.57^{+0.087}_{-0.077}$ ,

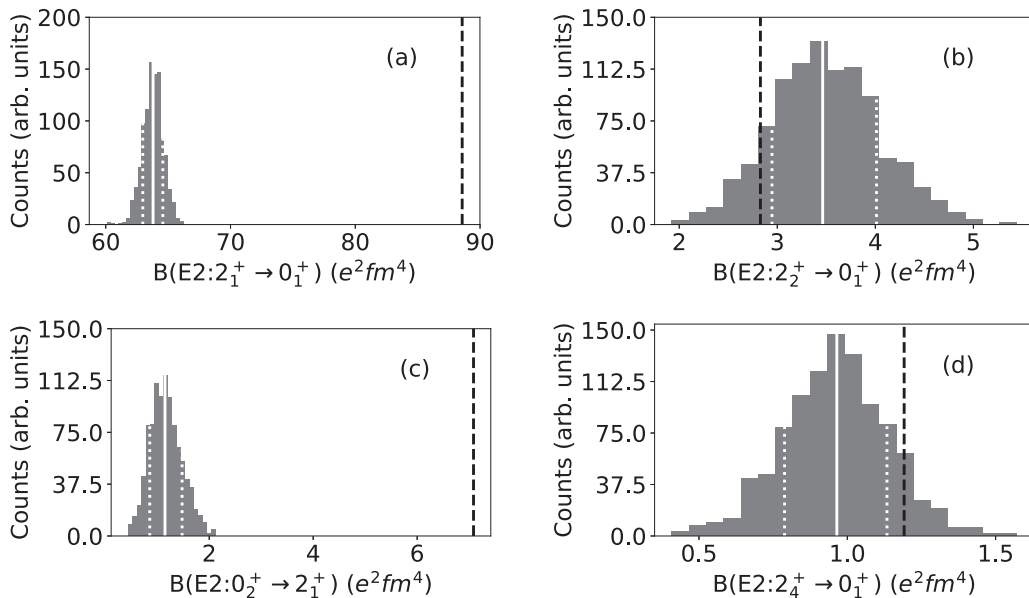


FIG. 5. Distributions of the electric quadrupole (E2) transition strengths for  $^{26}\text{Mg}$ . Black dashed line shows experimental value [39]. The median values and uncertainty interval are highlighted in white: (a)  $2_1^+ \rightarrow 0_1^+$ :  $63.7^{+0.78}_{-0.83}$ , (b)  $2_2^+ \rightarrow 0_1^+$ :  $3.46^{+0.55}_{-0.52}$ , (c)  $0_2^+ \rightarrow 2_1^+$ :  $1.15^{+0.33}_{-0.29}$ , (d)  $2_4^+ \rightarrow 0_1^+$ :  $0.96^{+0.18}_{-0.18}$ , all in units of  $e^2\text{fm}^4$ .

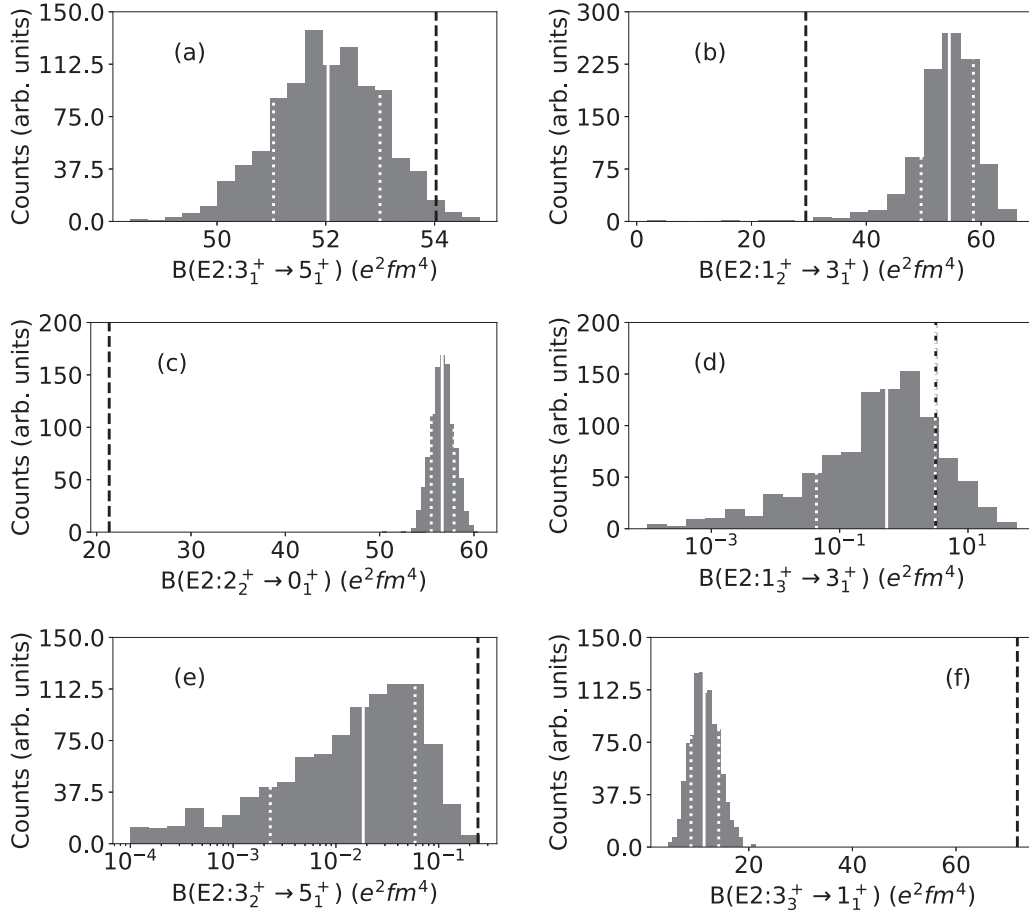


FIG. 6. Distributions of the electric quadrupole (E2) transition strengths for  $^{26}\text{Al}$ . Black dashed line shows experimental value [39]. The median values and uncertainty intervals are highlighted in white: (a)  $3_1^+ \rightarrow 5_1^+$ :  $52.04^{+0.99}_{-1.0}$ , (b)  $1_2^+ \rightarrow 3_1^+$ :  $54.47^{+4.19}_{-4.92}$ , (c)  $2_2^+ \rightarrow 0_1^+$ :  $56.63^{+1.26}_{-1.16}$ , (d)  $1_3^+ \rightarrow 3_1^+$ :  $0.53^{+2.53}_{-0.49}$ , (e)  $3_2^+ \rightarrow 5_1^+$ :  $0.017^{+0.041}_{-0.015}$ , and (f)  $3_3^+ \rightarrow 1_1^+$ :  $11.38^{+2.82}_{-2.53}$ , all in units of  $e^2 fm^4$ .

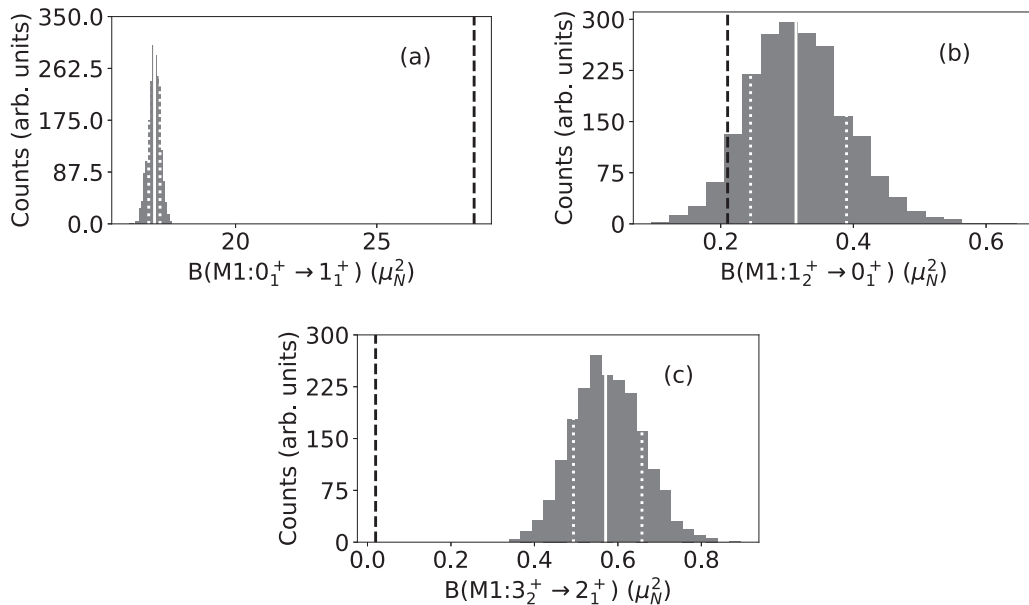


FIG. 7. Distributions of the magnetic dipole transition strengths for  $^{18}\text{F}$ . Black dashed line shows experimental value [40]. The uncertainty interval is highlighted in white: (a)  $0_1^+ \rightarrow 1_1^+$ :  $17.13^{+0.19}_{-0.21}$ , (b)  $1_2^+ \rightarrow 0_1^+$ :  $0.31^{+0.076}_{-0.068}$ , and (c)  $3_2^+ \rightarrow 2_1^+$ :  $0.57^{+0.087}_{-0.077}$ , all in units  $\mu_N^2$ .

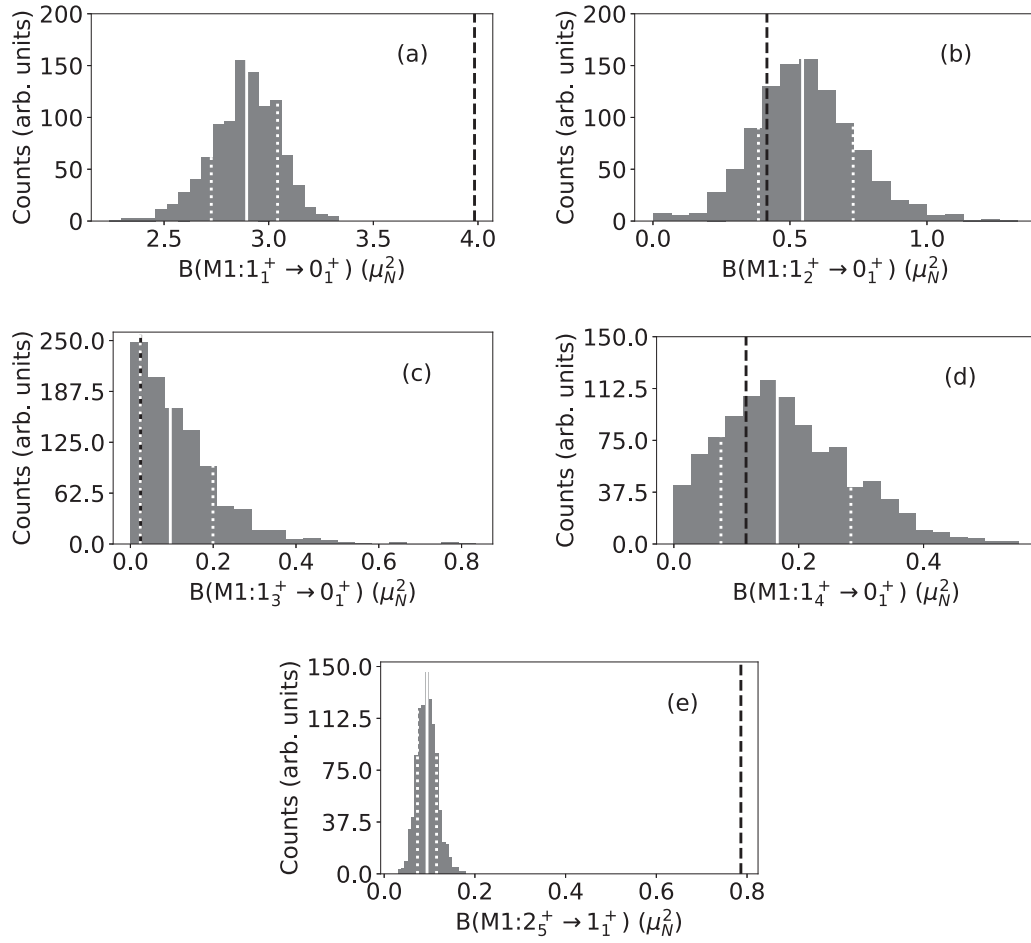


FIG. 8. Distributions of the magnetic dipole transition strengths for  $^{26}\text{Al}$ . Black dashed line shows experimental value [39]. The uncertainty interval is highlighted in white: (a)  $1_1^+ \rightarrow 0_1^+$  :  $2.89^{+0.15}_{-0.17}$ , (b)  $1_2^+ \rightarrow 0_1^+$  :  $0.55^{+0.18}_{-0.16}$ , (c)  $1_3^+ \rightarrow 0_1^+$  :  $0.096^{+0.10}_{-0.07}$ , (d)  $1_4^+ \rightarrow 0_1^+$  :  $0.17^{+0.12}_{-0.09}$ , and (e)  $2_5^+ \rightarrow 1_1^+$  :  $0.095^{+0.022}_{-0.021}$ , all in units  $\mu_N^2$ .

all in units  $\mu_N^2$ , where  $\mu_N$  is the nuclear magneton, while for  $^{26}\text{Al}$ , in Fig. 8 the median values and uncertainty intervals for our selected transitions are  $1_1^+ \rightarrow 0_1^+$  :  $2.89^{+0.15}_{-0.17}$ ,  $1_2^+ \rightarrow 0_1^+$  :  $0.55^{+0.18}_{-0.16}$ ,  $1_3^+ \rightarrow 0_1^+$  :  $0.096^{+0.10}_{-0.07}$ ,  $1_4^+ \rightarrow 0_1^+$  :  $0.17^{+0.12}_{-0.09}$ , and  $2_5^+ \rightarrow 1_1^+$  :  $0.095^{+0.022}_{-0.021}$ .

We show Gamow-Teller matrix elements for  $\beta^-$  decays in  $^{26}\text{Ne}$  and  $^{32}\text{Si}$  in Figs. 9 and 10, respectively. We have used for the axial-vector coupling constant  $g_A/g_V = -1.251$ , following Ref. [29], and a quenching factor of 0.76 for USDB. For  $^{26}\text{Ne}$ , in Fig. 9, the median values and uncertainty intervals for our selected transitions are  $0_1^+ \rightarrow 1_1^+$  :  $0.726^{+0.038}_{-0.037}$ ,  $0_1^+ \rightarrow 1_2^+$  :  $0.267^{+0.029}_{-0.030}$ , and  $0_1^+ \rightarrow 1_3^+$  :  $0.22^{+0.034}_{-0.037}$ , all unitless. The ground-state decay of  $^{32}\text{Si}$  has a small experimental transition strength, so our sensitivity analysis does not provide a normal distribution for B(GT). Using USDB, our median value and uncertainties are  $0.00597^{+0.0071}_{-0.0045}$ , but this is quite different than the experimental value is of 0.000038 [41]. This particular transition is very sensitive to the parameters: for the 1985 universal  $sd$ -shell interaction (USD) interaction [42] we get a value for B(GT) = 0.00005, and if one uses the 2006 universal  $sd$ -shell interaction version A (USDA), which is a less constrained version of USDB [22], the B(GT) is 0.038.

(Motivated by the non-Gaussian distribution in Fig. 10, we increased the number of samples from 1000 to 4000. The results were nearly indistinguishable, with new median value and uncertainties of  $0.00624^{+0.0077}_{-0.0047}$ .)

One of the biggest questions in physics today is the nature of nonbaryonic dark matter [43]. While there are a number of ongoing and planned experiments [44], interpreting experiments, including limits, requires good knowledge of the dark matter-nucleus scattering cross-section, including uncertainties. While historically it was assumed dark matter would couple either to the nucleon density or spin density, more recent work based upon effective field theory showed there should be a large number of low-energy couplings, around 15 [45]. This enlarged landscape of couplings, and the increased need for good theory, is a strong motivation for the current work.

To illustrate the application of UQ to nuclear matrix elements for dark matter scattering, Fig. 11 shows the uncertainty of an  $\vec{l} \cdot \vec{s}$  coupling for  $^{36}\text{Ar}$ .  $^{36}\text{Ar}$  is a small component (0.3%) of argon dark matter detectors, e.g., Ref. [46], but it is within the scope of the current work to compute. Of the EFT operators that do not vanish for a  $J^\pi = 0^+$  ground state, most of them depend upon radial wave functions that do not play a role



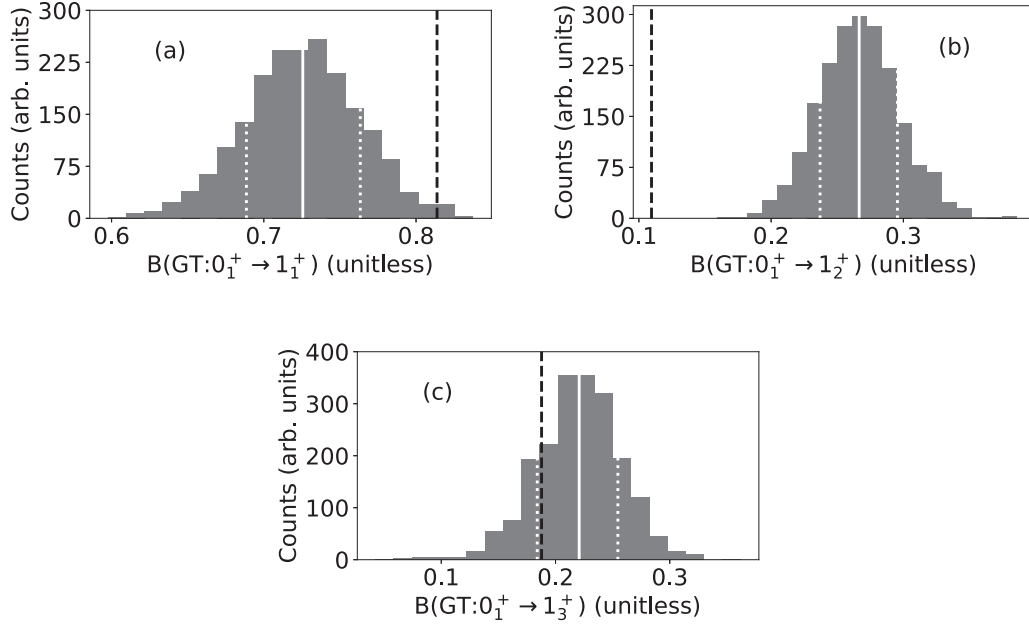


FIG. 9. Distributions of the Gamow-Teller (GT) transition strengths for  $\beta^-$ -decay of  $^{26}\text{Ne}$  to  $^{26}\text{Na}$ . Black dashed line shows experimental value [39]. The uncertainty interval is highlighted in white: (a)  $0_1^+ \rightarrow 1_1^+$  :  $0.726^{+0.038}_{-0.037}$ , (b)  $0_1^+ \rightarrow 1_2^+$  :  $0.267^{+0.029}_{-0.030}$ , and (c)  $0_1^+ \rightarrow 1_3^+$  :  $0.22^{+0.034}_{-0.037}$ .

in fitting the USDB parameters; nontrivial operators, however, include  $\vec{l} \cdot \vec{s}$ , which arises in the long-wavelength (momentum transfer  $q \rightarrow 0$ ) limit of the nuclear matrix elements of the operators  $\mathcal{O}_{3,12,15}$  [45]

$$\begin{aligned} \mathcal{O}_3 &= i\vec{s}_N \cdot \left( \frac{\vec{q}}{m_N} \times \vec{v}^\perp \right), \\ \mathcal{O}_{12} &= \vec{s}_\chi \cdot (\vec{s}_N \times \vec{v}^\perp), \\ \mathcal{O}_{15} &= -\left( \vec{s}_\chi \cdot \frac{\vec{q}}{m_N} \right) \left( (\vec{s}_N \times \vec{v}^\perp) \cdot \frac{\vec{q}}{m_N} \right), \end{aligned}$$

where  $m_N$  is the nucleon mass,  $\vec{q}$  is the momentum transfer,  $\vec{s}_{N/\chi}$  are the spins of the nucleon/WIMP, and  $\vec{v}^\perp$  is the component of the nucleon-WIMP relative velocity perpendicular to  $\vec{q}$ . We chose to study  $\langle \vec{l} \cdot \vec{s} \rangle$  for the simple reason of best illustrating a variance due to uncertainty in the USDB parameters. The variance of this particular operator is relatively small, but in larger model spaces there could be greater uncertainty.

Knowledge of the variance of the operator is important for interpreting experiments, such as placing upper limits on dark matter-nucleon couplings.

## V. CONCLUSIONS

We have carried out uncertainty quantification of a ‘‘gold-standard’’ empirical interaction for nuclear configuration-interaction calculations in the  $sd$ -shell valence. Rather than finding the uncertainty in each parameter independently [13], we computed the linear sensitivity of the energies, which is easy to compute using the Feynman-Hellmann theorem, and then constructed an approximate Hessian which we then diagonalized. This is equivalent to a singular-value decomposition of the linear sensitivity and is also known as principle component analysis. We found evidence this is a good approximation to the full Hessian. From the inverse of the diagonal (in a basis of the PCA linear combination of parameters) approximate Hessian, we obtained approximately

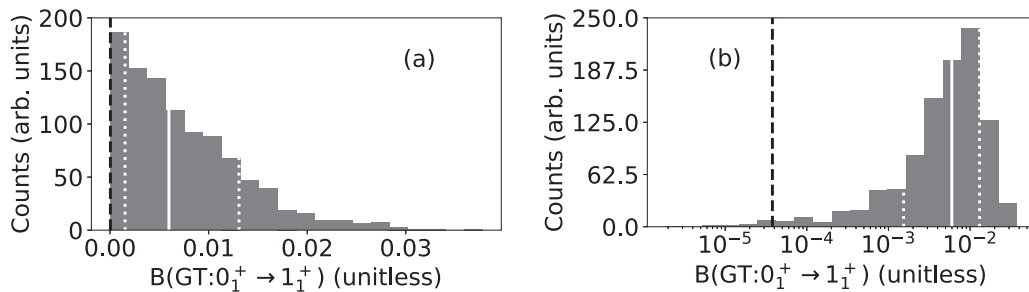


FIG. 10. Distribution of the Gamow-Teller (GT) transition strength for  $\beta^-$  decay of  $^{32}\text{Si}$  to  $^{32}\text{P}$  ( $0_1^+ \rightarrow 1_1^+$ ). The left plot is a linear scale in B(GT) and the right is log-scale. Black dashed line shows experimental value of 0.000038 [41]. The uncertainty interval is highlighted in white:  $0.00597^{+0.0071}_{-0.0045}$ .

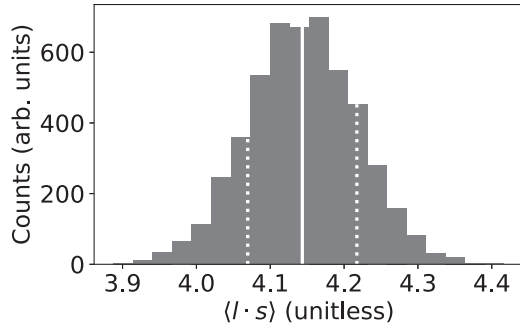


FIG. 11. Distribution of  $\langle l \cdot s \rangle$  in the ground-state of  $^{36}\text{Ar}$ . The  $1\sigma$  interval is highlighted in white:  $4.143 \pm 0.074$ .

independent uncertainties in the PCA parameters. Then, starting from those uncertainties, we generated uncertainties for energies as well as several observables. The distribution of residuals in energies implies statistical agreement, as well as an underlying systematic uncertainty in the shell model of 150 keV. For electromagnetic and weak transitions, which we note are sensitive to effective parameters such as effective charges and assumed oscillator length parameters, our residuals relative to experiment included both good agreement as well as residuals with statistically significant deviations. We also presented as a test case a dark matter-nucleus interaction matrix element and our derived uncertainty.

In the Supplemental Material [47], we provide the list of energies, courtesy of B. A. Brown, to which USDB was fit, and the eigenvalues and eigenvectors of our principal component analysis.

In future work, in addition to further and more systematic study of observables, we will carry out a more detailed and thorough study of parameter covariances, as well as applying our methods to other empirical interactions in other model spaces. This will entail, following Appendix A, evaluating the posterior without Laplace's approximation, and instead using Markov-chain Monte Carlo sampling. We are investigating the use of eigenvector continuation [48–50] to explore parameter space efficiently. For the time being, however, it seems that this approximate Hessian is a good approximation. This is not surprising, but it is useful. Nonetheless, moving to larger spaces, which grow exponentially in dimensions and compute time, will be challenging. New technologies still in development, such as quantum computing may make possible better and more rigorous uncertainty quantification.

#### ACKNOWLEDGMENTS

We thank B. Alex Brown for a helpful file of the energies to which USDB was fit, and S. Yoshida for further discussion and encouragement to look at the full calculation of the Hessian. G. W. Misch suggested we look at the transitions of  $^{26}\text{Al}$ , which have astrophysical relevance, and M. Horoi pointed out the  $\beta$ -decay of  $^{32}\text{Si}$  as a known case of sensitivity to the interaction. This material is based upon work supported by the U.S. Department of Energy, Office of Science, Office of Nuclear Physics, under Awards No. DE-FG02-96ER40985 (for nuclear structure) and No. DE-SC0019465 (for dark

matter matrix elements). J.F. thanks the Computational Science Research Center for partial support.

#### APPENDIX A: THE BAYESIAN CONTEXT

Our development above is cast in terms of standard sensitivity analysis. To connect with more sophisticated UQ analyses, and to set the stage for future work, we provide a broader, Bayesian context.

To define uncertainty on the USDB parameters, we start with Bayes' theorem. Let  $D$  represent data and  $\lambda$  the parameters, then

$$P(\lambda|D) = \frac{P(D|\lambda)P(\lambda)}{P(D)} \propto P(D|\lambda)P(\lambda). \quad (\text{A1})$$

Bayes' theorem states that the distribution of model parameters given the experimental data [the *posterior* =  $P(\lambda|D)$ ] is proportional to the distribution of data [the *likelihood* =  $P(D|\lambda)$ ] given the parameter set, multiplied by the *a priori* distribution of parameters [the *prior* =  $P(\lambda)$ ]. Bayesian analysis [51] demands that we put some thought into the choice of prior, and the typical choice here is a *noninformative* prior, which seeks to minimize the effects of prior knowledge on the posterior distribution. In this case a noninformative prior can simply be uniform and very broad in the limiting case,  $P(\lambda) = \text{constant}$  everywhere. This assigns equal probability to all parameter values (the principle of indifference [51]). Although one could also justify using an informative prior, the flat prior it is a sensible first approximation for the scope of this analysis.

With the prior set to constant, Bayes' theorem reduces to

$$P(\lambda|D) \propto P(D|\lambda). \quad (\text{A2})$$

The goal now is to evaluate this expression, and we can choose between two methods: Laplace's Approximation (LA) or Markov chain Monte Carlo (MCMC). Due to its simplicity, we choose LA, as did a prior shell-model study [13]. While MCMC advantageously makes no assumption as to the form of  $P(\lambda|D)$ , it typically converges slowly for posteriors which are steep around extrema, so the computational cost of LA is comparatively much less.

Laplace's approximation is a second-order Taylor approximation in the log-likelihood, and thus we assume normally distributed errors on energies. Our likelihood function takes the form

$$P(D|\lambda) = \exp\left[-\frac{1}{2}\chi^2(\lambda)\right], \quad (\text{A3})$$

where  $\chi^2$  is the usual sum of squared residuals:

$$\chi^2(\lambda) = \sum_{\alpha=1}^N \left( \frac{E_{\alpha}^{\text{SM}}(\lambda) - E_{\alpha}^{\text{exp}}}{\Delta E_{\alpha}} \right)^2. \quad (\text{A4})$$

$E_{\alpha}^{\text{exp}}$  is the experimental excitation energy given in the data set and  $E_{\alpha}^{\text{SM}}(\lambda)$  is the shell-model prediction for that energy using the parameters  $\lambda$ , with total uncertainty on the residual  $\Delta E_{\alpha}$  [see discussion in Sec. III and in particular Eq. (6)].

By Eq. (A3), there exists a global maximum of this likelihood function, called the maximum likelihood estimator (MLE). The optimal point for the posterior is called the

“maximum *a posteriori*” (MAP), and here we see that  $\lambda_{\text{MAP}} = \lambda_{\text{MLE}}$ , but of course this is only in the special case of uniform prior. In this work, the MAP is equal to the USDB parameters:

$$\begin{aligned}\lambda_{\text{MAP}} &= \underset{\lambda}{\operatorname{argmax}} P(\lambda|D) = \underset{\lambda}{\operatorname{argmax}} P(D|\lambda)P(\lambda) \\ &= \underset{\lambda}{\operatorname{argmin}} \chi^2(\lambda) = \lambda_{\text{USDB}}.\end{aligned}\quad (\text{A5})$$

The virtue of LA is we can immediately write down a properly normalized Gaussian approximation of the posterior:

$$P(\lambda|D) \approx \frac{|H|^{1/2}}{(2\pi)^{k/2}} \exp\left[-\frac{1}{2}(\lambda - \lambda_{\text{MAP}})^T H (\lambda - \lambda_{\text{MAP}})\right], \quad (\text{A6})$$

where  $k$  is the dimension of the parameter space, and  $H$  denotes the Hessian of the log-posterior (for brevity we refer to this as “the Hessian”). The Hessian is defined as minus the second-derivative (in  $\lambda$ ) of the log-likelihood about the MAP:

$$H = -\nabla\nabla \log P(\lambda|D)|_{\lambda=\lambda_{\text{MAP}}}. \quad (\text{A7})$$

Because of Eq. (A2), we can introduce an arbitrary constant  $c$ , so  $P(\lambda|D) = cP(D|\lambda)$ :

$$\begin{aligned}H &= -\nabla\nabla \log P(\lambda|D) = -\nabla\nabla \log cP(D|\lambda) \\ &= 0 - \nabla\nabla \log P(D|\lambda) = +\frac{1}{2}\nabla\nabla \chi^2(\lambda),\end{aligned}\quad (\text{A8})$$

so the elements of  $H$  become

$$H_{ij} = \frac{1}{2} \frac{\partial^2 \chi^2(\lambda)}{\partial \lambda_i \partial \lambda_j}. \quad (\text{A9})$$

Under these assumptions, we proceed as described in the main text.

## APPENDIX B: COMPUTED COVARIANCE OF FITTED ENERGIES

Here we show that computing the covariance matrix of fit energies  $C_E$  by Eq. (21) is simply related to a similarity transform of the original uncertainties on fit energies given by Eq. (6):  $\Sigma_{\alpha\alpha} = \Delta E_{\alpha}$ . The response of the energies to changes in the parameters is an  $N_d \times N_p$  Jacobian matrix,  $J_{\alpha i} = \partial E_{\alpha} / \partial \lambda_i$ , where  $N_d$  is the number of data points and  $N_p$  is the number of parameters. The approximate Hessian is

$$A = J^T \Sigma^{-2} J, \quad (\text{B1})$$

and the parameter covariance is

$$C_{\lambda} = A^{-1} = (J^T \Sigma^{-2} J)^{-1}. \quad (\text{B2})$$

Since  $J$  is not square, we cannot evaluate this expression in terms of matrix inversion and instead use the pseudoinverse obtained by SVD decomposition. We get the factorization  $J = USV^T$  where  $U$  is a  $N_d \times N_d$  unitary matrix,  $S$  is a  $N_d \times N_p$  matrix with the only nonzero elements being  $N_p$  singular values along the diagonal, and  $V$  is a  $N_p \times N_p$  unitary matrix. We use this to define a new matrix  $J^+$  which is the pseudoinverse of  $J$ :

$$J^+ = VS^+U^T. \quad (\text{B3})$$

Here,  $S^+$  is the pseudoinverse of  $S$ , which has the same shape as  $S^T$  and the only nonzero elements are such that  $S_{jj}^+ = 1/S_{jj}$  for  $j = 1, 2, \dots, N_p$ .

Plugging this into the expression for  $C_{\lambda}$  we have

$$C_{\lambda} = J^+ \Sigma^2 [J^T]^+ = (VS^+U^T) \Sigma^2 (US^+V^T). \quad (\text{B4})$$

In turn we insert this into our expression for  $C_E$ :

$$C_E = (USV^T)(VS^+U^T) \Sigma^2 (US^+V^T)(VSU^T). \quad (\text{B5})$$

By the orthogonality of  $U$  and  $V$  we have  $U^T U = I_d$  and  $U^T U = I_p$ , identity matrices in the data-space and parameter-space, respectively, so that

$$C_E = USI_p S^+ U^T \Sigma^2 U S^+ I_p S U^T. \quad (\text{B6})$$

To simplify further, we need to pay attention to the rank-deficient property of  $S$ . Define  $S I_p S^+ = P_d^p$  to be a  $N_d \times N_d$  square matrix with  $N_p$  1's on the diagonal, starting from the top, and all zeros otherwise. (This is projection operator from the data-space into the parameter-space, hence this notation.) Then

$$C_E = U P_d^p U^T \Sigma^2 U P_d^p U^T. \quad (\text{B7})$$

Now, notice that since  $\Sigma^2$  is diagonal, we have  $U^T \Sigma^2 U = \Sigma^2$ . The matrix  $P_d^p$  is of course idempotent so  $P_d^p P_d^p = P_d^p$ , and we get

$$C_E = U \Sigma^2 P_d^p U^T \quad (\text{B8})$$

or

$$U^T C_E U = \Sigma^2 P_d^p. \quad (\text{B9})$$

Thus, the computed covariance on the energies  $C_E$  is equivalent to a similarity transform of the input uncertainties  $\Sigma^2$ , albeit with rank =  $N_p$ .

## APPENDIX C: THE ROTATED QUANTILE-QUANTILE PLOT

The quantile-quantile (Q-Q) plot [52] is a useful tool for visualizing how well the distribution of a data set matches that of a random variate from a known probability distribution. Our *rotated* Q-Q plot in Fig. 2 shows the comparison of energy residuals to a standard normal distribution. The following gives a brief explanation.

A typical Q-Q plot graphs  $N$  measured data points  $\{x_i^{\text{data}}\}$ , sorted from lowest to highest, against  $N$  uniformly distributed evaluations  $\{x_i^{\text{eval}}\}$  of the *quantile function* (sometimes called a *percent-point function*) of the distribution we wish to compare to. For a random variable  $X$  with cumulative distribution function (CDF)  $F_X(x) \equiv \Pr(X \leq x)$ , the quantile function  $Q_X(p)$  returns the value of  $x$  such that  $F_X(x) = p$ ; in other words, it is the inverse function of the CDF. For instance if the set of data points follows a normal distribution, that is,  $\{x_i^{\text{eval}}\} = \{x_i^{\text{normal}}\}$  then the points  $(x_i^{\text{data}}, x_i^{\text{normal}})$  for  $i = 1, 2, \dots, N$  will fall on a straight line with slope of 1. If the data does not follow a normal distribution, then the points will deviate from a straight line, displaying how nonnormal the data is. Our Q-Q plot in Fig. 2 in this paper has been “rotated” by plotting instead  $(x_i^{\text{data}} - x_i^{\text{normal}}, x_i^{\text{normal}})$ , where  $x_i^{\text{data}}$  are the energy residuals, so that a normal distribution would lie on the

horizontal axis at zero. This allows for an easier identification of discrepancies between empirical and theoretical quantiles via visual inspection.

Many statistical tests exist for determining normality of data, and often these can be represented as a curve on the

Q-Q plot. The Kolmogorov-Smirnov and tail-sensitive tests used in this work correspond to curves shown in Fig. 2; evidence of possible nonnormality of the data is indicated by the plotted quantile-quantile points crossing over these curves.

- 
- [1] J. Dobaczewski, W. Nazarewicz, and P. Reinhard, *J. Phys. G: Nucl. Part. Phys.* **41**, 074001 (2014).
- [2] K. Wendt, B. Carlsson, and A. Ekström, [arXiv:1410.0646](https://arxiv.org/abs/1410.0646) (2014).
- [3] R. Furnstahl, D. Phillips, and S. Wesolowski, *J. Phys. G: Nucl. Part. Phys.* **42**, 034028 (2015).
- [4] B. D. Carlsson, A. Ekström, C. Forssén, D. F. Strömberg, G. R. Jansen, O. Lilja, M. Lindby, B. A. Mattsson, and K. A. Wendt, *Phys. Rev. X* **6**, 011019 (2016).
- [5] R. N. Pérez, J. Amaro, and E. R. Arriola, *Int. J. Mod. Phys. E* **25**, 1641009 (2016).
- [6] J. A. Melendez, R. J. Furnstahl, D. R. Phillips, M. T. Pratala, and S. Wesolowski, *Phys. Rev. C* **100**, 044001 (2019).
- [7] S. Wesolowski, R. Furnstahl, J. Melendez, and D. Phillips, *J. Phys. G: Nucl. Part. Phys.* **46**, 045102 (2019).
- [8] A. E. Lovell, F. M. Nunes, J. Sarich, and S. M. Wild, *Phys. Rev. C* **95**, 024611 (2017).
- [9] R. Navarro Pérez and J. Lei, *Phys. Lett. B* **795**, 200 (2019).
- [10] N. Schunck, J. D. McDonnell, D. Higdon, J. Sarich, and S. Wild, *Nucl. Data Sheets* **123**, 115 (2015).
- [11] J. D. McDonnell, N. Schunck, D. Higdon, J. Sarich, S. M. Wild, and W. Nazarewicz, *Phys. Rev. Lett.* **114**, 122501 (2015).
- [12] Y. Jaganathen, R. M. Id Betan, N. Michel, W. Nazarewicz, and M. Płoszajczak, *Phys. Rev. C* **96**, 054316 (2017).
- [13] S. Yoshida, N. Shimizu, T. Togashi, and T. Otsuka, *Phys. Rev. C* **98**, 061301(R) (2018).
- [14] P. Navrátil, J. P. Vary, and B. R. Barrett, *Phys. Rev. C* **62**, 054311 (2000).
- [15] B. R. Barrett, P. Navrátil, and J. P. Vary, *Prog. Part. Nucl. Phys.* **69**, 131 (2013).
- [16] U. van Kolck, *Phys. Rev. C* **49**, 2932 (1994).
- [17] P. Brussard and P. Glaudemans, *Shell-Model Applications in Nuclear Spectroscopy* (North-Holland Publishing Company, Amsterdam, 1977).
- [18] B. A. Brown and B. H. Wildenthal, *Annu. Rev. Nucl. Part. Sci.* **38**, 29 (1988).
- [19] E. Caurier, G. Martinez-Pinedo, F. Nowack, A. Poves, and A. P. Zuker, *Rev. Mod. Phys.* **77**, 427 (2005).
- [20] G. Hagen, T. Papenbrock, D. J. Dean, and M. Hjorth-Jensen, *Phys. Rev. C* **82**, 034330 (2010).
- [21] S. R. Stroberg, H. Hergert, S. K. Bogner, and J. D. Holt, *Annu. Rev. Nucl. Part. Sci.* **69**, 307 (2019).
- [22] B. A. Brown and W. A. Richter, *Phys. Rev. C* **74**, 034315 (2006).
- [23] C. W. Johnson and P. G. Krastev, *Phys. Rev. C* **81**, 054303 (2010).
- [24] H. Hellman, *Einführung in die Quantenchemie* (Franz Deutick, Leipzig und Wien, 1937), p. 285.
- [25] R. P. Feynman, *Phys. Rev.* **56**, 340 (1939).
- [26] R. R. Whitehead, A. Watt, B. J. Cole, and I. Morrison, in *Advances in Nuclear Physics*, edited by M. Baranger and E. Vogt (Plenum, 1977), p. 123.
- [27] C. W. Johnson, W. E. Ormand, and P. G. Krastev, *Comput. Phys. Commun.* **184**, 2761 (2013).
- [28] C. W. Johnson, W. E. Ormand, K. S. McElvain, and H. Shan, [arXiv:1801.08432](https://arxiv.org/abs/1801.08432) (2018).
- [29] W. A. Richter, S. Mkhize, and B. A. Brown, *Phys. Rev. C* **78**, 064302 (2008).
- [30] W. A. Richter and B. A. Brown, *Phys. Rev. C* **80**, 034301 (2009).
- [31] L. Lyons, *Statistics for Nuclear and Particle Physicists* (Cambridge University Press, Cambridge, UK, 1989).
- [32] L. Montanet, K. Gieselmann, R. M. Barnett, D. E. Groom, T. G. Trippe, C. G. Wohl, B. Armstrong, G. S. Wagman, H. Murayama, J. Stone, J. J. Hernandez, F. C. Porter, R. J. Morrison, A. Manohar, M. Aguilar-Benitez, C. Caso, P. Lantero, R. L. Crawford, M. Roos, N. A. Törnqvist, K. G. Hayes, G. Höhler, S. Kawabata, D. M. Manley, K. Olive, R. E. Shrock, S. Eidelman, R. H. Schindler, A. Gurtu, K. Hikasa, G. Conforto, R. L. Workman, and C. Grab ( Particle Data Group), *Phys. Rev. D* **50**, 1173 (1994).
- [33] W. H. Press, S. A. Teukolsky, W. T. Vetterling, and B. P. Flannery, *Numerical Recipes in Fortran 77: The Art of Scientific Computing*, Vol. 2 (Cambridge University Press, Cambridge, UK, 1992).
- [34] Kolmogorov–Smirnov test, in *The Concise Encyclopedia of Statistics* (Springer, New York, NY, 2008), pp. 283–287.
- [35] R. Navarro Pérez, J. E. Amaro, and E. Ruiz Arriola, *J. Phys. G: Nucl. Phys.* **42**, 034013 (2015).
- [36] S. Aldor-Noiman, L. D. Brown, A. Buja, W. Rolke, and R. A. Stine, *Am. Stat.* **67**, 249 (2013).
- [37] R. N. Perez, E. Garrido, J. E. Amaro, and E. Ruiz Arriola, *Phys. Rev. C* **90**, 047001 (2014).
- [38] R. Navarro Pérez, J. E. Amaro, E. Ruiz Arriola, P. Maris, and J. P. Vary, *Phys. Rev. C* **92**, 064003 (2015).
- [39] M. Basunia and A. Hurst, *Nucl. Data Sheets* **134**, 1 (2016).
- [40] D. Tilley, H. Weller, C. Cheves, and R. Chasteler, *Nucl. Phys. A* **595**, 1 (1995).
- [41] C. Ouellet and B. Singh, *Nucl. Data Sheets* **112**, 2199 (2011).
- [42] B. Brown and B. Wildenthal, *At. Data Nucl. Data Tables* **33**, 347 (1985).
- [43] G. Bertone and D. Hooper, *Rev. Mod. Phys.* **90**, 045002 (2018).
- [44] L. Roszkowski, E. M. Sessolo, and S. Trojanowski, *Rep. Prog. Phys.* **81**, 066201 (2018).
- [45] N. Anand, A. L. Fitzpatrick, and W. C. Haxton, *Phys. Rev. C* **89**, 065501 (2014).
- [46] P. Agnes, T. Alexander, A. Alton, K. Arisaka, H. Back, B. Baldin, K. Biery, G. Bonfini, M. Bossa, A. Brigatti *et al.*, *Phys. Lett. B* **743**, 456 (2015).
- [47] See Supplemental Material at <http://link.aps.org/supplemental/10.1103/PhysRevC.101.054308> for the list of energies and the eigenvalues and eigenvectors of our principal component analysis.

- [48] D. Frame, R. He, I. Ipsen, D. Lee, D. Lee, and E. Rrapaj, *Phys. Rev. Lett.* **121**, 032501 (2018).
- [49] A. Ekström and G. Hagen, *Phys. Rev. Lett.* **123**, 252501 (2019).
- [50] S. König, A. Ekström, K. Hebeler, D. Lee, and A. Schwenk, *arXiv:1909.08446* (2019).
- [51] D. S. Sivia and J. Skilling, *Data Analysis: A Bayesian Tutorial*, 2nd ed. (Oxford Science Publications, Oxford, UK, 2006).
- [52] 1.3.3.24: Quantile-quantile plot, in *NIST/SEMATECH e-Handbook of Statistical Methods* (NIST, 2013), <http://www.itl.nist.gov/div898/handbook/>.